J. Fluid Mech. (1979), *vol.* 90, *part* 1, *pp.* 109–127
Printed in Great Britain

Vortex breakdown in a rotating cylindrical cavity

By J. M. OWEN AND J. R. PINCOMBE
School of Engineering and Applied Sciences, University of Sussex,
Falmer, Brighton BN1 9QT, England

(Received 26 April 1977 and in revised form 4 April 1978)

Flow visualization, laser-Doppler anemometry and pressure measurements have been used to identify and delineate the regimes of vortex breakdown in a rotating cavity with a central axial flow of air. For the particular cavity tested (where the ratio of the outer to the inner radius was ten and the ratio of the axial width to the inner radius was approximately five), spiral breakdown and axisymmetric breakdown occur in both laminar and turbulent flow. Rossby numbers ϵ characterizing the boundaries between the breakdown modes were established from visual observations of flow behaviour, from discontinuities in velocity components and in the pressure drop across the cavity, and from changes in the velocity spectra. In laminar flow, spiral breakdown occurs for $1{\cdot}5 \lesssim \epsilon \lesssim 3{\cdot}2$ and axisymmetric breakdown occurs for $0{\cdot}8 \lesssim \epsilon \lesssim 1{\cdot}5$. In turbulent flow, spiral breakdown occurs for $21 \lesssim \epsilon \lesssim 100$ and $1{\cdot}5 \lesssim \epsilon \lesssim 2{\cdot}6$, and axisymmetric breakdown occurs for $2{\cdot}6 \lesssim \epsilon \lesssim 21$ and $0{\cdot}8 \lesssim \epsilon \lesssim 1{\cdot}5$. At the higher Rossby numbers, the flow under laminar conditions is significantly different to that under turbulent conditions; at the lower Rossby numbers, it was found to be impossible to distinguish between laminar and turbulent flow.

1. Introduction

During an experimental programme in which heat-transfer measurements were made inside a rotating cylindrical cavity with an axial throughflow of coolant (see figure 1), Owen & Bilimoria (1977) observed that relatively small changes in rotational speed or axial flow rate could, under certain conditions, cause dramatic increases in heat-transfer rates. Using flow visualization with a Perspex model of the heat-transfer rig, it was found that over certain ranges of the Rossby number ϵ ($\epsilon \equiv \overline{W}/\Omega a$, $\overline{W}$ being the bulk average axial velocity in the inlet pipe) the central jet ceased to be axisymmetric and precessed violently about its axis. This behaviour, which was attributed to vortex breakdown, caused a large increase in the circulation within the cylindrical cavity and, in the heat-transfer rig, was responsible for the dramatic increases in heat-transfer rates.

A similar phenomenon was also reported by Yu, Sparrow & Eckert (1973), who observed, for turbulent flow, an asymmetric precession of the jet in a cylindrical cavity in which one disk rotated and the second disk and the cylindrical shroud were stationary. In their experiments, the coolant entered at the centre of the rotating disk (through a rotating tube 'via a circumferential array of narrow longitudinal slots') and left through a radial clearance between the stationary disk and the shroud. An examination of these results reveals that for the cavity geometries examined ($b/a = 10$, $4 < s/a < 20$) spiral breakdown, or precession of the jet, occurred in the

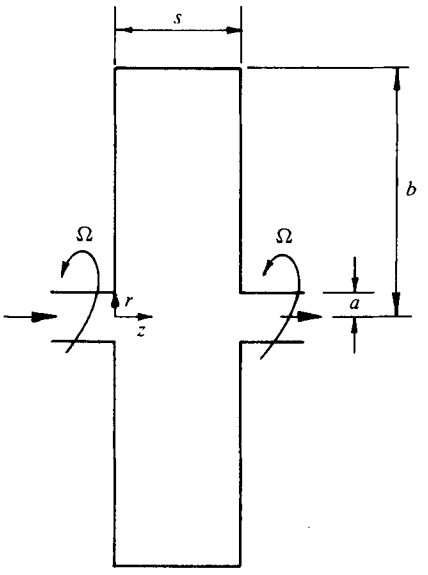

FIGURE 1. Schematic diagram of a rotating cylindrical cavity with an axial throughflow.

Rossby number range $1{\cdot}2 < \epsilon < 12$. During spiral breakdown, the frequency of the jet precession was found to be independent of disk rotational speed. For $\epsilon < 1{\cdot}2$, the flow was axisymmetric but separation occurred on the jet axis.

According to the comprehensive review by Hall (1972), vortex breakdown (an abrupt change in the structure of a swirling axial flow) is associated with three main factors. These are (i) a large upstream swirl angle ϕ ($\tan\phi \equiv v/w$, v and w being the local values of the tangential and axial components of velocity, respectively) of the order of 40° or greater, (ii) an adverse axial pressure gradient and (iii) divergence of the stream tubes in the vortex core immediately upstream of the breakdown. These three effects are normally present during vortex breakdown, and their relative magnitudes determine the form that the breakdown takes.

Most studies of vortex breakdown have been concerned with vane-induced swirl in conical or cylindrical stationary ducts. Experiments in cylindrical ducts were conducted by Harvey (1962), for laminar flow, and by Kirkpatrick (1964), for turbulent flow. Both these authors found that the maximum swirl angle (which occurred at a radial distance of about one-third of the duct radius upstream of the breakdown) was approximately 50°. Sarpkaya (1971) observed that, for laminar flow in a diffusing duct, the vortex breakdown could have either an axisymmetric form or an asymmetric spiral form. The axisymmetric breakdown (in which a separation bubble formed on the axis of the duct) was found to be the limiting case of the spiral breakdown as the angle between the vane and the axial direction was increased. At smaller vane angles, spiral breakdown occurred and the maximum upstream swirl angle varied from 38 to 50°; as the vane angle was increased, axisymmetric breakdown occurred with a maximum upstream swirl angle of approximately 50°; further increases in the vane angle did not increase the swirl angle nor alter the form of the breakdown. Sarpkaya also observed that there was a hysteresis region in which the spiral and axisymmetric breakdowns were unstable and could commute.

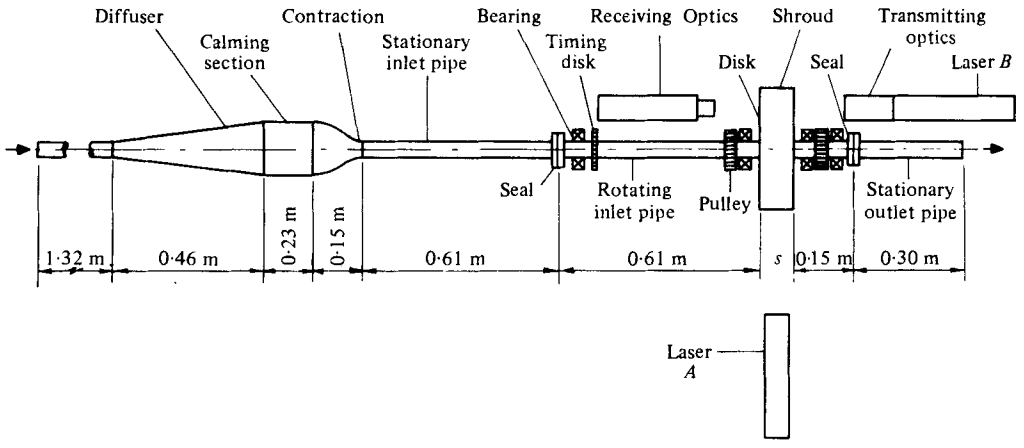

FIGURE 2. Schematic arrangement of the experimental apparatus.

There is, at present, no universally accepted theoretical explanation of vortex breakdown although two models, put forward by Benjamin (1962, 1967) and by Mager (1972), have been widely applied to flow in stationary ducts. Both models are consistent with the results of Sarpkaya (1971), although recent numerical solutions of the Navier–Stokes equations by Grabowski & Berger (1976) support the Mager, rather than the Benjamin, model.

There has been, to the authors' knowledge, no attempt to predict the onset or nature of vortex breakdown in rotating cavities, and it is not the object of this paper to provide a theoretical description of breakdown phenomena. The aim of the authors is to draw attention to vortex breakdown in rotating cavities and to provide some interesting and, it is believed, important experimental results. It is hoped that the data presented will be used to test existing theoretical models and to stimulate the development of new ones.

The experimental apparatus is described briefly in § 2, and the reader is referred to Owen & Pincombe (1977) if more details of the equipment or instrumentation are required. Sections 3, 4, 5 and 6 discuss, respectively, the results of flow visualization, velocity measurements by laser-Doppler anemometry, pressure measurements and spectral analysis of the fluctuations within the cavity.

2. Experimental apparatus

2.1. *Rotating disk assembly and flow facility*

A schematic diagram of the apparatus is given in figure 2 and a photograph of the disk assembly is shown in figure 3 (plate 1).

The rotating cavity comprised two annular Perspex disks, of outer radius $b = 190\,\text{mm}$, sealed at the outer radii with a cylindrical Perspex shroud. Each disk was attached at its inner radius to a stainless-steel tube of inner radius $a = 19\,\text{mm}$. The whole disk assembly could be rotated at values of Re_θ up to 4×10^5 ($Re_\theta \equiv \Omega b^2/\nu$) by a variable-speed electric motor, and the speed, which was steady to within 1 %, could be measured to an accuracy of 1 rev/min by means of a magnetic transducer

and a timer–counter. The axial spacing between the two disks could be adjusted up to a maximum of $s = 100$ mm. This maximum clearance, which produced a gap ratio of $s/a = 5{\cdot}3$, was used for all of the tests described below.

As illustrated in figure 2, air was supplied to the disk assembly from a pipe, of bore 38 mm, connected by means of a diffuser to a calming section. The calming section, of diameter 152 mm, contained four gauze screens followed by a 16 : 1 area-ratio contraction which was designed to produce a flat low-turbulence velocity profile in the stationary inlet pipe. The inlet and outlet pipes were of bore 38 mm, and leakage between the rotating and stationary sections was prevented by 'V-ring' seals. In an attempt to generate solid-body rotation in the approach flow, provision was made for the insertion of a matrix of small tubes at the upstream end of the rotating inlet tube. The tube matrix comprised 60 thin-walled tubes of diameter 4 mm and length 200 mm.

Axial Reynolds numbers up to $Re_z \simeq 10^5$ ($Re_z \equiv 2\overline{W}a/\nu$) were obtained from a centrifugal fan. The flow rate was determined by Annubar differential pressure-sensing elements located upstream of the diffuser. The pressure drop across the cavity was measured between two static pressure tappings located in the stationary pipes immediately upstream and downstream of the rotating inlet and outlet pipes. The pressure difference across the cavity, and across the Annubar for low flow rates, was measured by an electromanometer with a resolution of 0·01 mm W.G. The pressure difference across the Annubar for high flow rates was measured by a micromanometer with a resolution of 0·1 mm W.G. From calibrations with positive displacement meters, the flow rate could be measured to an accuracy of better than 3 %.

For flow visualization, the air flow was 'seeded' by means of a smoke generator, which vaporized large volumes of oil particles (approximately 0·8 μm in diameter) that were injected upstream of the calming section. For the laser anemometry, a micro-fog lubricator was used to atomize oil particles of diameter approximately 2 μm or less. According to Melling & Whitelaw (1973), an oil particle of diameter 2 μm should be able to follow turbulent fluctuations with an error of less than 1 % for frequencies up to 2 kHz. Using the relationships of Burson, Keng & Orr (1967), for solid-body rotation the 'radial migration error' (or ratio of the particle radial velocity to the tangential air velocity) will be less than 0·2 % for the measurements reported below.

2.2. *Optical instrumentation*

Flow visualization was used to obtain a qualitative picture of the flow inside the cavity; laser-Doppler anemometry was used to measure the radial, tangential and axial components of velocity.

For flow visualization, a $\frac{1}{2}$ mW He–Ne laser (laser A in figure 2) was used in conjunction with a cylindrical lens to produce illumination of either the r, θ or the r, z plane of the cylindrical cavity. By seeding the air with oil particles, the flow patterns were readily observable.

The laser-Doppler anemometer (LDA) comprised transmitting and receiving optics, arranged in a forward-scatter real-fringe mode as shown in figure 3, and a Cambridge Consultants' tracking filter. Early tests were conducted without frequency shifting; later tests used a rotating diffraction grating to provide frequency shifting for measurements of the highly turbulent, three-dimensional, recirculating flow inside the cavity.

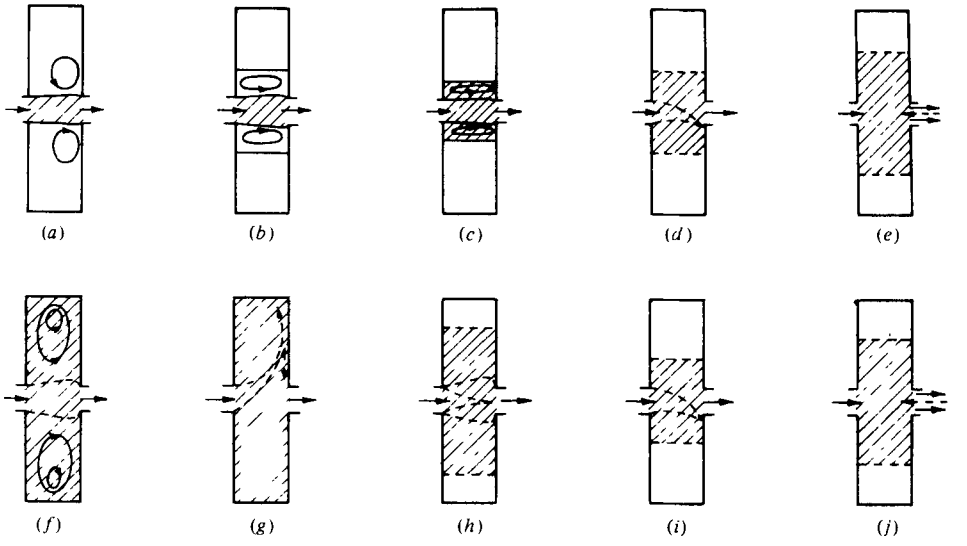

FIGURE 4. Visual impressions of the flow inside a rotating cylindrical cavity.

	(a)	(b)	(c)	(d)	(e)	(f)	(g)	(h)	(i)	(j)
Rossby number	∞	25	4	2	1	∞	25	4	2	1
	Laminar flow, $Re_z = 3000$					Turbulent flow, $Re_z = 5000$				

The tracking filter output (a voltage proportional to the fluid velocity component being measured) was passed into either a digital integrating voltmeter or a digital spectrum analyser. The former provided true time-average and r.m.s. values ('proportional' to the time-average velocity component and turbulence intensity); the latter produced the power spectrum of the measured velocity component.

3. Flow visualization

By illuminating the r, z plane and pulsing the smoke generator, it was possible to observe the behaviour of the main axial jet and the secondary flow in the cavity. In the visual impression in figure 4, shading is used to represent regions where smoke penetrated quickly by convection (rather than slowly by diffusion) and dashed lines are used to imply intermittency or uncertainty.

For a stationary cavity, laminar flow could be readily identified by observing the jet boundary. For $Re_z < 7000$ (with no 'trip' downstream of the contraction), the boundary was well defined over almost the entire length of the jet. For $Re_z \approx 7000$, fluctuations at the downstream end of the jet shed vortices into the cavity but these were quickly damped out; at $Re_z \approx 1{\cdot}3 \times 10^4$, the downstream half of the jet boundaries were fluctuating and vortices shed into the cavity were no longer damped out; at $Re_z \approx 2 \times 10^4$, the entire jet boundary fluctuated and the secondary flow in the cavity was totally turbulent. By 'tripping' the flow downstream of the contraction (insertion of the tube matrix also tripped the flow), transition from laminar to turbulent flow started at $Re_z \approx 2300$.

Owing to the unsteady nature of the flow during vortex breakdown, there was no

convenient way of distinguishing laminar from turbulent flow during rotation. Sections 3.1 and 3.2 describe flows that were laminar and turbulent, respectively, in the stationary cavity.

3.1. *Laminar flow*

Figure 4(*a*) illustrates an idealization of laminar flow in the stationary cavity. In practice, owing to the comparative weakness of the secondary flow, a temperature difference of less than 0·1 °C between the cavity walls and the air was sufficient to generate buoyancy forces that destroyed the axisymmetry and distorted the secondary toroidal vortex.

The lack of symmetry was attenuated by rotation, and for $Re_z = 3000$, $3{\cdot}2 \lesssim \epsilon < \infty$, increasing the rotational speed caused the toroidal vortex to shrink towards the centre, creating a core of smoke, as shown in figures 4(*b*) and (*c*). For a given Rossby number, the size of the smoke core was found to increase with increasing Re_z.

At $\epsilon \approx 3{\cdot}2$, the main jet became unstable and produced a 'flickering flame' effect, as illustrated in figure 4(*d*). Oscillations of the jet caused an increase in the size of the smoke core, the increase being greater at the smaller Re_z and negligible for $Re_z > 5000$. The behaviour of the jet, which will be termed mode I vortex breakdown, appears to be similar to the spiral breakdown described by Sarpkaya (1971).

The spiral behaviour was observed for $1{\cdot}5 \lesssim \epsilon \lesssim 3{\cdot}2$ (the precise values depending to some extent on the value of Re_z). At $\epsilon \lesssim 1{\cdot}5$, there was evidence of occasional flow reversal at the downstream end of the jet, with an increase of smoke penetration into the cavity. This behaviour, which is illustrated in figure 4(*e*), is similar to Sarpkaya's axisymmetric breakdown and will be termed mode II vortex breakdown.

The occurrence and severity of the mode II disturbances reached a peak at $\epsilon \approx 0{\cdot}8$ and for smaller Rossby numbers there was another dramatic change in the flow structure. A reduction of the smoke core occurred and a periodic wave motion appeared on the jet boundaries, but the onset of this effect at $\epsilon \approx 0{\cdot}8$ was sensitive to small temperature variations. Owing to the high rotational speeds required, and the need for precise thermal controls, no detailed experiments were conducted for $\epsilon < 0{\cdot}8$.

In the above tests, which were conducted without the tube matrix inserted, the beginning of mode I was subject to a hysteresis effect, and there was an uncertainty in the mode I to mode II boundary where both forms of breakdown appeared to coexist. With the matrix inserted, modes I and II were observed over similar ranges of Rossby number to those specified above; however, with the matrix, the effects of breakdown were weaker and the regions of uncertainty were greater.

3.2. *Turbulent flow*

For the stationary cavity, transition from laminar to turbulent flow was associated with increased entrainment at the jet boundary and a dramatic increase in the circulation within the cavity. For turbulent flow, a powerful axisymmetric toroidal vortex centred at $r/a \approx 8$, $z/s \approx 0{\cdot}5$ caused smoke to fill the entire cavity, as shown in figure 4(*f*).

No obvious effect of rotational speed was observed until $\epsilon \approx 100$, where an occasional precession of the main jet about the central axis was seen. As the Rossby number was further reduced, the jet precession occurred more regularly and eventually became continuous. The form of breakdown, which is similar to the behaviour reported by

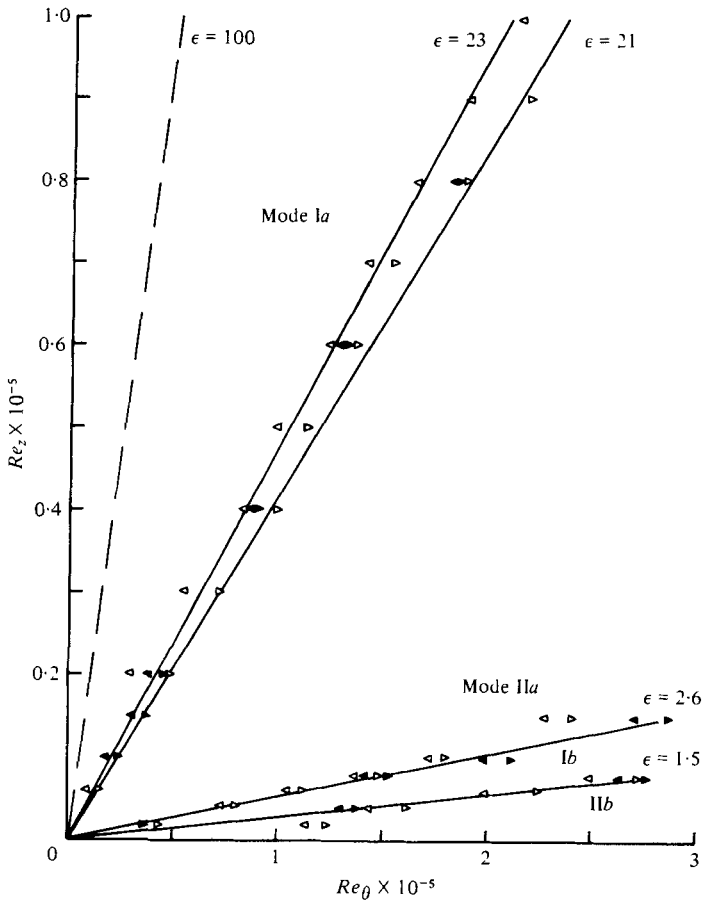

FIGURE 5. Regimes of vortex breakdown in a rotating cylindrical cavity with turbulent axial throughflow. ▷, Re_θ increasing, no matrix; ◁, Re_θ decreasing, no matrix; ▶, Re_θ increasing, with matrix; ◀, Re_θ decreasing, with matrix.

Yu *et al.* (1973), is shown in figure 4 (*g*) and will be referred to as mode I*a*. The amplitude of the jet's precession increased to reach a maximum at $\epsilon \approx 21$, whereafter, at higher rotational speeds, the jet suddenly stopped precessing. If for $\epsilon < 21$, when the jet had resumed its central position, the Rossby number was increased (by speed reduction or by flow increase), the jet did not resume its precession until $\epsilon \gtrsim 23$.

For $\epsilon < 21$, the jet appeared to be axisymmetric with occasional oscillations of the jet boundaries, and this will be referred to as mode II*a*. Occasional excursions of the jet into the cavity were observed, and for $\epsilon \lesssim 10$, an inner core of smoke with imprecise boundaries was formed as shown in figure 4 (*h*). As the Rossby number was further reduced, the smoke core continued to shrink and the occurrence of the jet's excursion into the cavity increased.

At $\epsilon \approx 2{\cdot}6$, the jet took on the 'flickering flame' appearance of the mode I laminar breakdown. The jet oscillations had a negligible effect on the size of the smoke core, and no further change in behaviour was observed until $\epsilon \approx 1{\cdot}5$. This effect, which will be referred to as mode I*b* breakdown, is shown in figure 4 (*i*).

At $\epsilon \approx 1{\cdot}5$, signs of intermittent reverse flow were observed at the downstream end

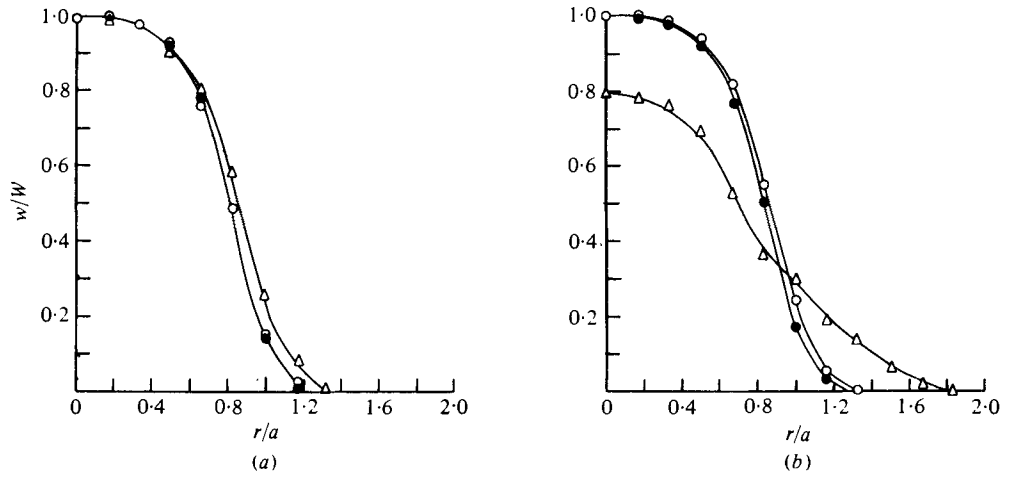

FIGURE 6. Axial velocity components in laminar flow, $Re_z = 3000$. (*a*) $z/s = 0{\cdot}251$. (*b*) $z/s = 0{\cdot}755$. —○—, $\epsilon = \infty$; —●—, $\epsilon = 3{\cdot}0$; —△—, $\epsilon = 1{\cdot}5$.

of the jet, similar to those seen in the mode II laminar breakdown. A further increase in speed caused the smoke core to increase in size to reach a maximum value at $\epsilon \approx 1$, and the breakdown, which will be referred to as mode II*b*, is shown in figure 4(*j*). As for the laminar flow, there was a dramatic reduction in the size of the smoke core at $\epsilon \approx 0{\cdot}8$, the resulting flow behaviour being dependent on the thermal conditions.

Figure 5 shows the regions of vortex breakdown when the flow was tripped to produce transition from laminar to turbulent flow, in the stationary cavity, at $Re_z \approx 2300$. Hysteresis was found between all the mode boundaries: the start of mode I at $\epsilon \approx 100$ was confirmed by the pressure measurements described in § 5; the boundaries between modes II*a* and I*b* and modes I*b* and II*b*, which were subject to hysteresis, were determined by the spectral analysis discussed in § 6; the boundaries between modes I*a* and II*a* were obtained from flow visualization.

With the tube matrix inserted, the effects were weaker and the boundaries were more difficult to define, although the modes of turbulent breakdown occurred over regions similar to those without the matrix.

4. Velocity measurements

4.1. *Laminar flow*

By placing the LDA along a radial line (with the transmission optics diametrically opposite the receiving optics and 'looking through' the shroud), it was possible to measure axial and tangential components of velocity near the centre of the cavity. For the axial components, the practicable region of traverse inside the cavity was limited to $0 < r/a < 2$, $0{\cdot}19 < z/s < 0{\cdot}83$; for the tangential components, the regime was limited to $0 < r/a < 2$, $0{\cdot}03 < z/s < 0{\cdot}97$. With the upstream disk removed, it was possible to measure the tangential component at $z/s = 0{\cdot}005$ for $0 < r/a < 1$. By placing the LDA along an axial line ('looking through' the disk), it was possible to measure radial and tangential components of velocity over the region $5{\cdot}3 < r/a < 9$, $0{\cdot}03 < z/s < 0{\cdot}97$. All measurements were conducted with $s/a = 5{\cdot}3$.

Figure 6 shows the radial distribution of the time-average axial component of

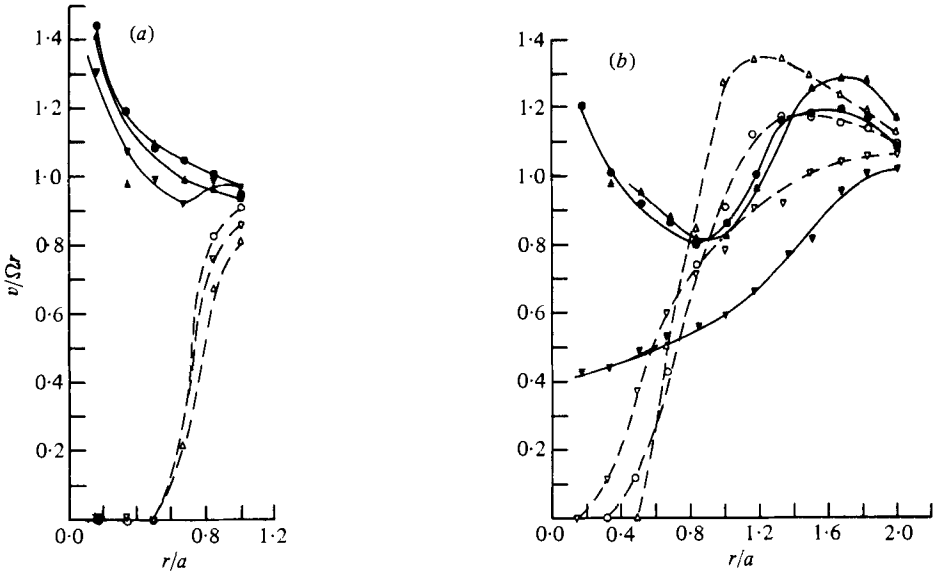

FIGURE 7. Tangential velocity components in laminar flow, $Re_z = 3000$. (*a*) $z/s \approx 0{\cdot}005$. (*b*) $z/s = 0{\cdot}5$. Without matrix: --△--, $\epsilon = 6$; --○--, $\epsilon = 3$; --▽--, $\epsilon = 1{\cdot}5$. With matrix: —▲—, $\epsilon = 6$; —●—, $\epsilon = 3$; —▼—, $\epsilon = 1{\cdot}5$.

velocity w (normalized with respect to W, the centre-line value for the stationary cavity) for laminar flow at $Re_z = 3000$, without the tube matrix inserted. At the two axial locations shown, the stationary centre-line values W were within 1 % of each other.

Figure 6 (*a*) shows that rotational speed has little effect on the velocity profile near the inlet to the cavity, but figure 6 (*b*) shows that near the outlet the profile exhibits a marked change at $\epsilon = 1{\cdot}5$. In fact, during mode I and mode II breakdowns, the centre-line value could be reduced to values $w/W < 0{\cdot}7$. During mode II breakdown, examination of the instantaneous velocity component showed occasional stagnation, but no reversal, on the central axis.

As the inlet tube was short, it was not possible to achieve fully developed velocity profiles. Without the tube matrix inserted, the tangential component of velocity was zero for $r/a < 0{\cdot}5$ at the entry to the cavity, as can be seen from figure 7 (*a*). It can also be seen that, although the swirl was considerably increased by the presence of the matrix, solid-body rotation was not produced in the jet for $r/a < 1$. (It should be noted that at $Re_z = 3000$ the flow with the matrix inserted was not strictly laminar.)

Figure 7 (*b*) shows the tangential velocity distribution in the axial centre of the cavity. For $r/a > 2$, the flow in the cavity approaches solid-body rotation and is little influenced by the presence or absence of the matrix. Measurements of the tangential velocity at $r/a > 5{\cdot}3$ revealed solid-body rotation with no measurable radial velocity component in the cavity. Like the axial components, the tangential components are time-average values.

4.2. *Turbulent flow*

Figure 8 shows the axial velocity component (again normalized relative to the centre-line value W for the stationary cavity) for turbulent flow, with $Re_z = 3{\cdot}2 \times 10^4$, at two

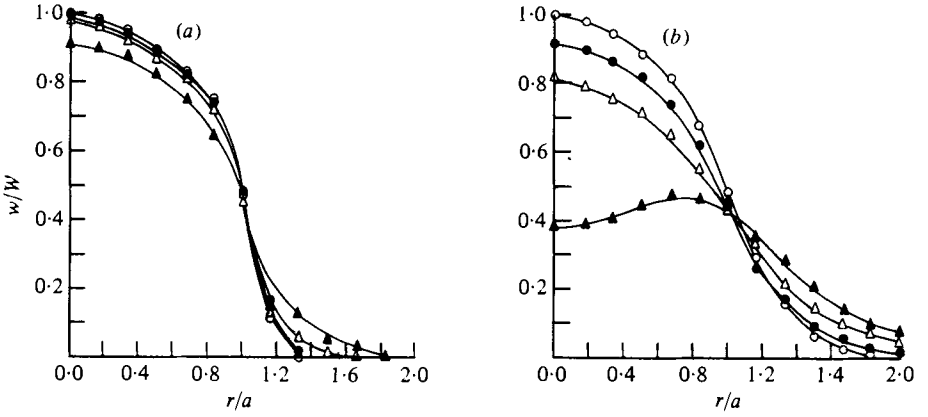

FIGURE 8. Axial velocity components in turbulent flow, $Re_z = 3{\cdot}2 \times 10^4$. (*a*) $z/s = 0{\cdot}251$. (*b*) $z/s = 0{\cdot}755$. ○, $\epsilon = \infty$; △, $\epsilon = 64$; ▲, $\epsilon = 28$; ●, $\epsilon = 16$.

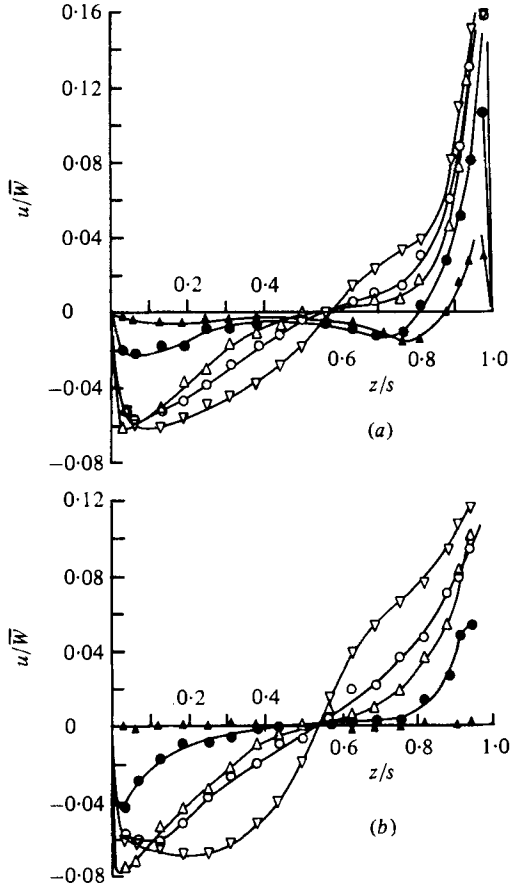

FIGURE 9. Radial velocity components in turbulent flow, $Re_z = 3{\cdot}2 \times 10^4$. (*a*) $r/a = 5{\cdot}7$. (*b*) $r/a = 8$. ▽, $\epsilon = \infty$; ○, $\epsilon = 128$; △, $\epsilon = 64$; ●, $\epsilon = 28$; ▲, $\epsilon = 16$.

axial locations. Near the inlet to the cavity, at $z/s = 0{\cdot}251$, it can be seen that the centre-line value is lower during mode Ia breakdown ($\epsilon = 64, 28$). Near the outlet from the cavity, at $z/s = 0{\cdot}755$, this effect is much more pronounced. Although the time-average values show no velocity reversal, the precessional motion of the jet at $\epsilon = 28$ is revealed by the velocity maximum occurring at $r/a \approx 0{\cdot}8$. These measurements are consistent with the observations in § 3 (and the spectral analysis discussed in § 6), where the jet precession was seen to build up progressively, with increasing rotational speed, from $\epsilon \simeq 100$ to reach a maximum at $\epsilon \simeq 21$, and to disappear for $\epsilon < 21$. During mode IIb breakdown, examination of the instantaneous velocity component revealed occasional velocity reversals on the centre-line, in agreement with the observations in § 3.2.

For turbulent flow, the secondary flow within the cavity is considerably more powerful than for laminar flow. The increased shear on the jet boundaries and the increased entrainment into the cavity create a toroidal vortex centred at $r/a \simeq 8$, $z/s \simeq 0{\cdot}5$. The effect of increasing rotational speed is to reduce the toroidal circulation as is shown by the measurements of the radial component of velocity in figure 9. The radial components are normalized with respect to the bulk-average axial velocity $\overline{W}$ at the inlet and are presented for $Re_z = 3{\cdot}2 \times 10^4$ and two radial locations. In figure 9(a), for $r/a = 5{\cdot}7$ (the minimum value of r/a for practicable traverses), the radial flow is outward near the downstream disk in the manner of a wall jet and inward near the upstream disk.

A number of experimental difficulties were experienced in measuring the radial components. These were principally caused by the high turbulence levels in the cavity and by the fact that, at high rotational speeds, the radial component was much smaller than the tangential component. Despite the difficulties (see Owen & Pincombe 1977), the calculated radial mass outflow rate (obtained by spatially integrating the time-average radial velocity component) was typically within a few per cent of the calculated inflow. However, at some conditions (for example at $\epsilon = 16$ in figure 9a), there are obvious errors.

The mass balances also reveal that, at any radial location, the radial outflow (and inflow) decreases with increasing rotational speed. For example, at $r/a = 8$ the radial mass flow rate decreases from a value nearly three times that of the central axial mass flow rate at $\epsilon = \infty$ to zero at $\epsilon = 16$. It should be noted that the relatively large radial flow rates result from the cross-sectional areas involved (which are large compared with that of the central hole) and not from the radial velocities (which are small compared with the central mean axial velocity). It is estimated (from the spatial integration of the time-average axial components of velocity near the centre of the cavity) that only a few per cent of the axial throughflow is entrained into, and out of, the cavity; the majority of the radial flow inside the cavity is caused by recirculation in the toroidal vortex.

It can be seen from figure 9(b) that for $\epsilon = 16$ the time-average radial velocity is virtually zero at $r/a = 8$. It was found that during mode IIa the radial velocity became zero at a radius that reduced with reducing Rossby number in a manner consistent with the reducing central core noted in § 3.2.

Figure 10 shows the axial distribution of the time-average tangential velocity component (normalized with respect to the local rotational speed of the cavity) for turbulent flow at $Re_z = 3{\cdot}2 \times 10^4$. In figure 10($a$), for $r/a = 5{\cdot}7$, it can be seen that the

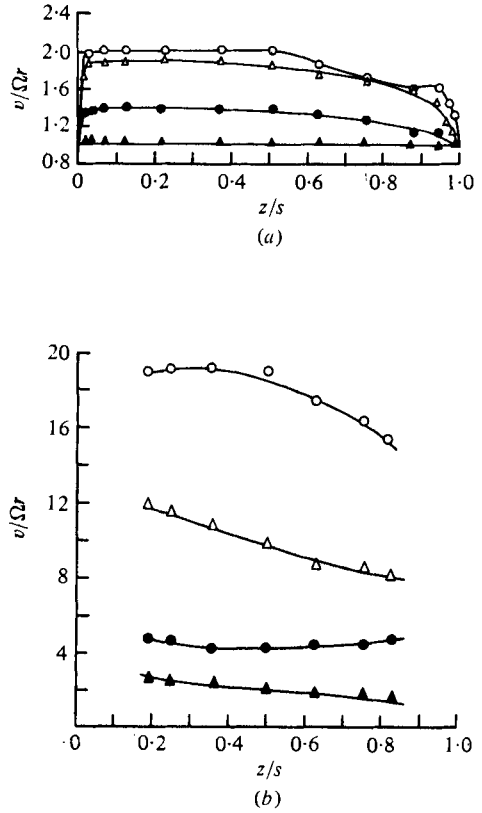

FIGURE 10. Tangential velocity components in turbulent flow, $Re_z = 3{\cdot}2 \times 10^4$. (*a*) $r/a = 5{\cdot}7$. (*b*) $r/a = 1{\cdot}5$. ○, $\epsilon = 128$, △, $\epsilon = 64$; ●, $\epsilon = 28$; ▲, $\epsilon = 16$.

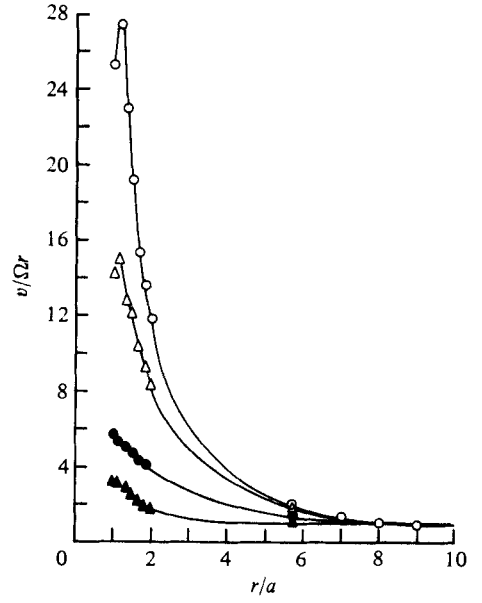

FIGURE 11. Tangential velocity components in turbulent flow, $Re_z = 3{\cdot}2 \times 10^4$, $z/s = 0{\cdot}189$. —○—, $\epsilon = 128$; —△—, $\epsilon = 64$; —●—, $\epsilon = 28$; —▲—, $\epsilon = 16$.

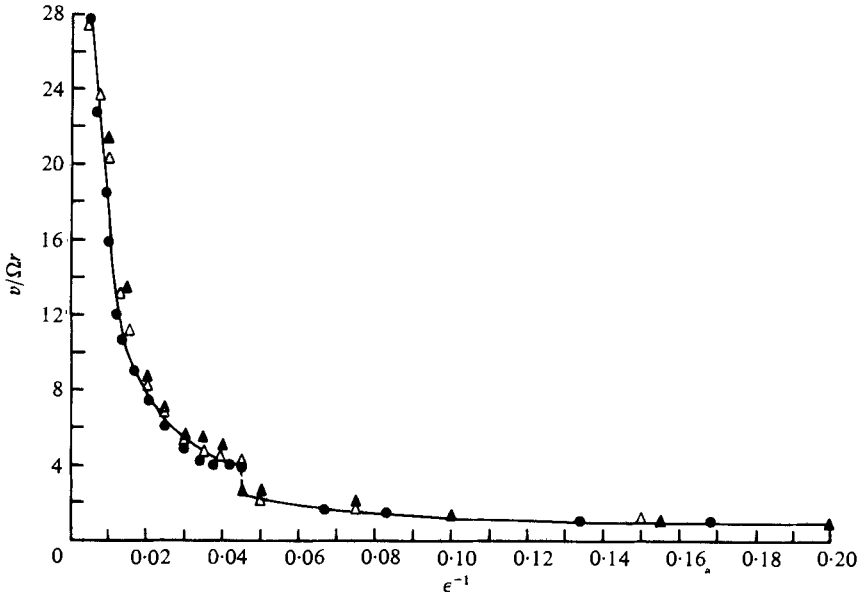

FIGURE 12. Tangential velocity components in turbulent flow, $r/a = 1{\cdot}33$, $z/s = 0{\cdot}189$. ▲, $Re_z = 1 \times 10^4$; △, $Re_z = 2 \times 10^4$; ●, $Re_z = 3 \times 10^4$.

effect of increasing rotational speed, or decreasing Rossby number, is to reduce the tangential velocity, which is always greater than or equal to the cavity speed. At radial locations nearer the axis this effect is more pronounced. Figure 10(*b*) shows that at $r/a = 1{\cdot}5$ the tangential velocity varies from a maximum of $v/\Omega r \simeq 19$ at $\epsilon = 128$ to $v/\Omega r \simeq 2{\cdot}4$ at $\epsilon = 16$. By contrast, it was found that for the outer radial locations, $8 < r/a < 10$, the tangential velocity was always less than or equal to the local cavity speed regardless of the Rossby number.

Outside the wall boundary-layer regions, the axial variation of the tangential velocity is less significant than the radial variation. The latter is illustrated in figure 11, which shows the radial variation of $v/\Omega r$ at an axial location $z/s = 0{\cdot}189$ for an axial Reynolds number Re_z of $3{\cdot}2 \times 10^4$. The radial distribution of tangential velocity lies between that of a free vortex and that of a forced vortex. At the larger Rossby numbers it tends to the former; at the lower Rossby numbers it tends to the latter. It would appear from figure 11 that a thin shear layer exists between the flow in the cavity and the jet. The flow in the cavity under these conditions is unlikely to be significantly different whether $v/\Omega r$ is unity or zero at $r = a$, an observation that is supported by the fact that only small differences were seen during flow visualization when the tube matrix was inserted or withdrawn. The measurements discussed above were, in fact, taken without the matrix inserted.

Figure 12 shows the variation of $v/\Omega r$ (measured at $r/a = 1{\cdot}33$ and $z/s = 0{\cdot}189$) with the inverse Rossby number for $Re_z = 1, 2$ and 3×10^4. The results show that the reduction of tangential velocity with increasing rotational speed (increasing values of ϵ^{-1}) is similar for all values of Re_z. In particular, there is a discontinuity at $\epsilon^{-1} \simeq 0{\cdot}045$ ($\epsilon \simeq 22$), which is consistent with the change from mode I*a* to mode II*a* breakdown observed in § 3.2.

As stated in § 1, vortex breakdown is associated with a critical swirl angle ϕ, an

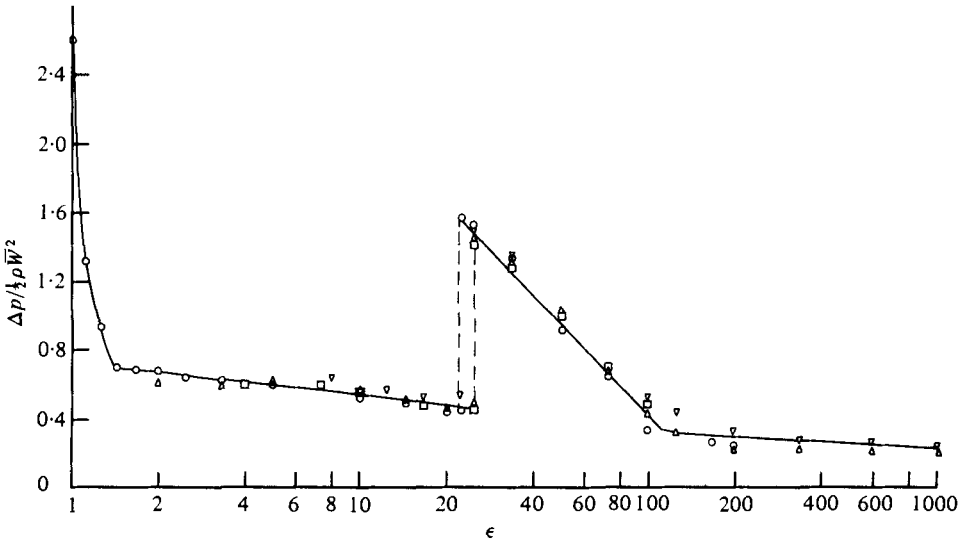

FIGURE 13. Pressure drop across the cavity in turbulent flow. ○, $Re_z = 1 \times 10^4$; △, $Re_z = 2 \times 10^4$; □, $Re_z = 4 \times 10^4$; ▽, $Re_z = 8 \times 10^4$.

adverse pressure gradient and divergence of the stream tubes upstream of breakdown. In Sarpkaya's (1971) experiments with vane-induced swirl, ϕ reached a maximum value of the order of 40–50° (at $r/a \approx 0{\cdot}3$) during breakdown. In the experiments described here, it was not practicable to measure ϕ directly; and the fact that the measured values of the axial and tangential components of velocity were time averaged militates against an accurate estimate of the swirl angle. Another difficulty in determining the variation of ϕ within the central jet is that the boundaries of the latter were difficult to determine with any accuracy. The boundaries diverged downstream of the inlet (and subsequently converged immediately upstream of the outlet) and, owing to the secondary flow within the cavity, the stagnation streamlines were experimentally indeterminate. However, from the results shown in figures 8, 11 and 12, it can be deduced that the swirl angle increases with increasing r/a, and near the jet boundaries ($1 < r/a < 1{\cdot}4$) ϕ is of the order of 40° and appears to remain approximately constant during mode Ia breakdown ($21 \lesssim \epsilon \lesssim 100$) regardless of the rotational speed or axial flow rate. The discontinuity in $v/\Omega r$ at $\epsilon^{-1} \simeq 0{\cdot}045$ (see figure 12) suggests that the swirl angle undergoes a step change in the transition from mode Ia to mode IIa breakdown.

The discontinuous behaviour in the tangential velocity during the transitional breakdown could be used to delineate modes Ia and IIa. The tangential velocity was measured at a fixed location and, whilst the rotational speed was held constant, the flow rate was varied until a step change in v occurred (at $\epsilon \simeq 21$). The values obtained in this way correlated well with the results shown on figure 5. The end of vortex breakdown for $\epsilon > 100$ did not result in an obvious discontinuity in velocity, and this change of regime was deduced from the pressure measurements described below.

5. Pressure measurements

As the static pressure tappings were located in the stationary tubes, upstream and downstream of the cavity, it was not possible to obtain a direct measurement of the pressure drop across the cavity itself. A number of tests were conducted, at $s/a = 5{\cdot}3$, by fixing the axial Reynolds number and measuring the pressure drop for a range of rotational speeds. The tests were then repeated with the disks pushed together ($s/a = 0$), in order to establish the pressure drop in the upstream and downstream tubes. The difference between the pressure drops for $s/a = 5{\cdot}3$ and $s/a = 0$ was assumed to be the pressure drop across the cavity itself.

As the pressure drop across the cavity was often smaller than the pressure drop in the rotating tubes, accurate measurements were difficult to obtain. The results discussed below are restricted to turbulent flow, without the tube matrix inserted, where the pressure drops were relatively large. An extended range was obtained by tripping the flow downstream of the contraction to promote transition at $Re_z \simeq 2300$. Owing to the unsteady nature of the pressure differences, particularly during vortex breakdown, the voltage output from the electromanometer was integrated to produce time-average values.

The derived pressure drop Δp across the cavity, non-dimensionalized with respect to the 'average dynamic pressure' $\frac{1}{2}\rho\overline{W}^2$, is plotted against the Rossby number in figure 13. In view of the assumptions made in deriving the pressure drop, and the errors in measuring it, the results for $10^4 < Re_z < 8 \times 10^4$ show a remarkably similar form, from which it can be concluded that the dimensionless pressure drop is a function of the Rossby number only.

The discontinuity at $\epsilon \approx 100$ is assumed to indicate the start of the mode Ia breakdown, and the step change for $22 \lesssim \epsilon \lesssim 25$ correlates well with the mode Ia/IIa boundary. There is no indication of the mode IIa/IIb boundary, but the sharp increase in pressure drop at $\epsilon \lesssim 1{\cdot}5$ is consistent with the mode IIb breakdown. Although it was difficult to obtain accurate results for $\epsilon < 1$, the pressure drop appeared to reach a peak at $\epsilon \approx 0{\cdot}8$ and decreased sharply for smaller Rossby numbers.

It should be noted that the dimensionless pressure drop across the stationary cavity was approximately 0·2.

6. Spectral analysis of the LDA signal

During measurements of the tangential component of velocity inside the cavity, the analog voltage output from the tracking filter was passed into the digital spectrum analyser. During vortex breakdown, there was good correlation between the visual observation of jet oscillations and the appearance of 'peaks' in the power spectrum of the velocity component. When it was possible to measure the frequency of the jet oscillations (for example, by timing the visually observed precession of the jet during mode Ia breakdown), close agreement was found between the timed results and the frequency of the spectral peak.

In laminar flow, mode I breakdown is associated with a dominant peak at a frequency of half the rotational frequency of the cavity. This is shown in figure 14(a), which shows the tangential component measured for $Re_z = 3000$ inside the cavity at $r/a = 5{\cdot}3$ and $z/s = 0{\cdot}5$. By contrast, mode II breakdown is associated with a peak

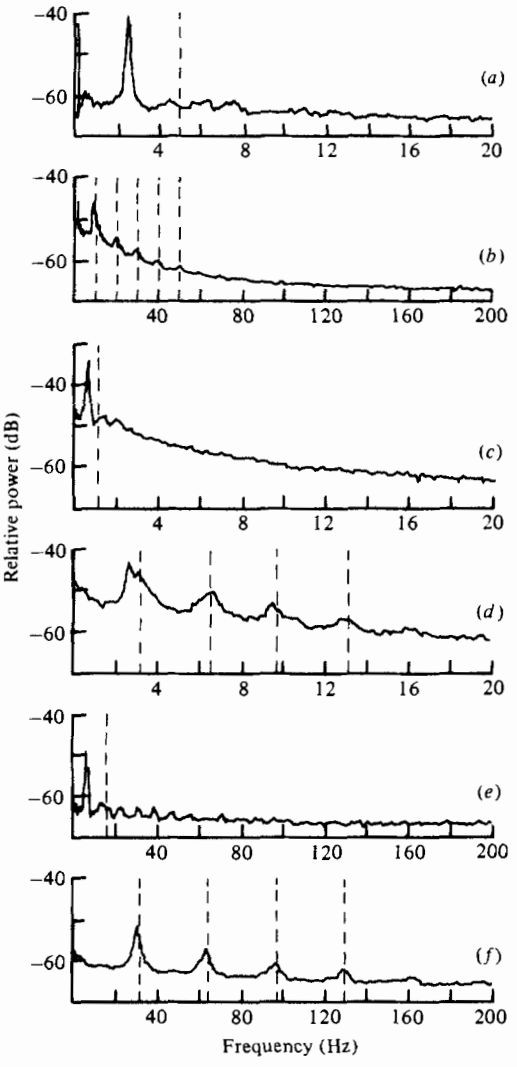

FIGURE 14. Power spectrum of the tangential component of velocity, $r/a = 5{\cdot}3$, $z/s = 0{\cdot}5$. (*a*), (*b*) $Re_z = 3000$ (laminar). (*c*)–(*f*) $Re_z = 10^4$ (turbulent). (*a*) $\epsilon = 2$. (*b*) $\epsilon = 1$. (*c*) $\epsilon = 30$. (*d*) $\epsilon = 10$. (*e*) $\epsilon = 2$. (*f*) $\epsilon = 1$. – – –, cavity rotational frequency and harmonics.

at the rotational frequency of the cavity together with a number of higher harmonics,† as is shown in figure 14(*b*).

In turbulent flow, mode I*a* breakdown produces a dominant peak similar to that observed in laminar flow. An example of the mode I*a* result is shown in figure 14(*c*) for $Re_z = 10^4$ (with the flow 'tripped'). By contrast, mode II*a* breakdown produces a peak at the cavity frequency together with higher harmonics, which, as can be seen from figure 14(*d*), is similar to the laminar axisymmetric breakdown case. As shown in figure 14(*e*), mode I*b* breakdown is similar to mode I*a*; and as shown in figure 14(*f*), mode II*b* is similar to mode II*a*. It would therefore appear that, from visual observa-

† The fact that these peaks were not caused by mechanical vibrations was verified by their disappearance when the air flow was turned off whilst the cavity was rotating.

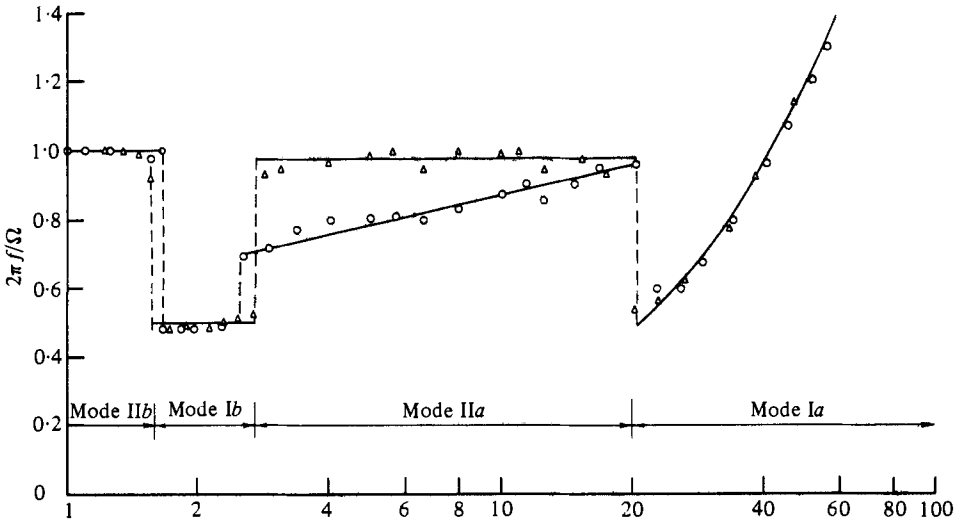

FIGURE 15. Relative frequency of the tangential velocity component in turbulent flow, $Re_z = 10^4$, $z/s = 0{\cdot}75$. ○, $r/a = 0{\cdot}83$; △, $r/a = 5{\cdot}3$.

tions and spectral analysis, the laminar spiral breakdown and turbulent breakdown modes Ia and Ib are related, as are the laminar axisymmetric breakdown and turbulent breakdown modes IIa and IIb. From visual and spectral evidence, it would appear that flow that is turbulent in the stationary cavity is laminarized at small Rossby numbers. The spectral 'signature' of the vortex breakdowns was used to delineate the mode IIa/Ib and the mode Ib/IIb boundaries in figure 5, although it should be pointed out that near boundaries spectra changed continuously without discontinuity.

During vortex breakdown, no significant difference was discerned between spectra obtained from tangential and axial components of velocity inside the main jet. The frequency f of the dominant peaks obtained from spectra of tangential components measured at $r/a = 0{\cdot}83$ and $r/a = 5{\cdot}3$ is plotted against the Rossby number in figure 15. The discontinuities between the breakdown modes can be clearly seen, and it can be deduced that the dominant frequency in the cavity (and, except for mode IIa, in the jet) is given by

$$2\pi f/\Omega \approx \begin{cases} 0{\cdot}024\epsilon & \text{for mode I}a, \\ 1 & \text{for modes II}a, \text{II}b, \\ 0{\cdot}5 & \text{for mode I}b. \end{cases}$$

It should be noted that during mode Ia breakdown the frequency of the jet oscillation is independent of the rotational speed of the cavity (as noted by Yu *et al.* 1973) but is proportional to the axial velocity such that

$$af/\overline{W} \approx 0{\cdot}0038.$$

In the case of the mode IIa breakdown the spectrum changed, progressively, from the single-peak behaviour (associated with spiral breakdown) at $r/a = 0{\cdot}83$ to the harmonic behaviour (associated with axisymmetric breakdown) at $r/a = 5{\cdot}3$.

The above results were obtained without the tube matrix inserted. The main effect of the matrix was to attenuate the spectral peaks without significantly affecting the positions of the boundaries between the various modes of vortex breakdown.

7. Conclusions

From experimental measurements inside a rotating cylindrical cavity (with a radius ratio $b/a = 10$ and a gap ratio $s/a = 5{\cdot}3$) with an axial throughflow of air, spiral and axisymmetric vortex breakdowns have been observed in both laminar and turbulent flow.

In laminar flow, spiral breakdown (which causes the jet to precess about the axis of the cavity) was observed for the Rossby number range $1{\cdot}5 \lesssim \epsilon \lesssim 3{\cdot}2$ and axisymmetric breakdown (where occasional stagnation occurs on the axis of the cavity) was observed for the range $0{\cdot}8 \lesssim \epsilon \lesssim 1{\cdot}5$. In turbulent flow, spiral breakdown occurred for $21 \lesssim \epsilon \lesssim 100$ and $1{\cdot}5 \lesssim \epsilon \lesssim 2{\cdot}6$ and axisymmetric breakdown occurred for $2{\cdot}6 \lesssim \epsilon \lesssim 21$ and $0{\cdot}8 \lesssim \epsilon \lesssim 1{\cdot}5$. At the larger Rossby numbers, the presence of breakdown in turbulent flow and its absence in laminar flow was attributed to large-scale structural flow differences, in the cavity and on the jet boundaries, between the turbulent and laminar flow: small-scale turbulent fluctuations (which increased the jet entrainment and hence affected the flow in the cavity) were only indirectly responsible for vortex breakdown. At the smaller Rossby numbers, it was not possible to distinguish between laminar and turbulent flow.

The boundaries between spiral and axisymmetric breakdown, with their associated hysteresis regions, were established by flow visualization, from discontinuities in velocity and pressure measurements and from changes in the velocity spectra. The spectral 'signature' revealed similarities between the spiral breakdowns in laminar and turbulent flow (and between the axisymmetric breakdowns) and differences between the spiral and axisymmetric breakdowns.

Whilst the cavity geometry and approach conditions might be expected to affect the regimes of vortex breakdown, varying degrees of inlet swirl had a relatively small effect on the occurrence, and nature, of the breakdown. Further work is necessary to establish the effect of the cavity gap ratio on the occurrence of vortex breakdown.

The authors wish to thank the Science Research Council for sponsoring the work described in this paper and to thank Dr R. H. Rogers for her advice and assistance.

REFERENCES

BENJAMIN, T. B. 1962 Theory of the vortex breakdown phenomenon. *J. Fluid Mech.* **14**, 593.

BENJAMIN, T. B. 1967 Some developments in the theory of vortex breakdown. *J. Fluid Mech.* **28**, 65.

BURSON, J. H., KENG, E. Y. H. & ORR, C. 1967 Particle dynamics in centrifugal fields. *Powder Tech.* **1**, 305.

GRABOWSKI, W. J. & BERGER, S. A. 1976 Solutions of the Navier–Stokes equations for vortex breakdown. *J. Fluid Mech.* **75**, 525.

HALL, M. G. 1972 Vortex breakdown. *Ann. Rev. Fluid Mech.* **4**, 195.

HARVEY, J. K. 1962 Some observations of the vortex breakdown phenomenon. *J. Fluid Mech.* **14**, 585.

KIRKPATRICK, D. L. I. 1964 Experimental investigation of the breakdown of a vortex in a tube. *R.A.E. Tech. Note* Aero 2963.

MAGER, A. 1972 Dissipation and breakdown of a wing-tip vortex. *J. Fluid Mech.* **55**, 609.

MELLING, A. & WHITELAW, J. H. 1973 Seeding of gas flows for laser anemometry. *DISA Inf.* **15**, 5.

OWEN, J. M. & BILIMORIA, E. D. 1977 Heat transfer in rotating cylindrical cavities. *J. Mech. Engng Sci.* **19**, 175.

OWEN, J. M. & PINCOMBE, J. R. 1977 Vortex breakdown in a rotating cylindrical cavity. *School Engng Appl. Sci., Univ. Sussex Rep.* no. 76/Me/79.

SARPKAYA, T. 1971 On stationary and travelling vortex breakdowns. *J. Fluid Mech.* **45**, 545.

YU, J. P., SPARROW, E. M. & ECKERT, E. R. G. 1973 Experiments on a shrouded parallel disk system with rotation and coolant throughflow. *Int. J. Heat Mass Transfer* **16**, 311.

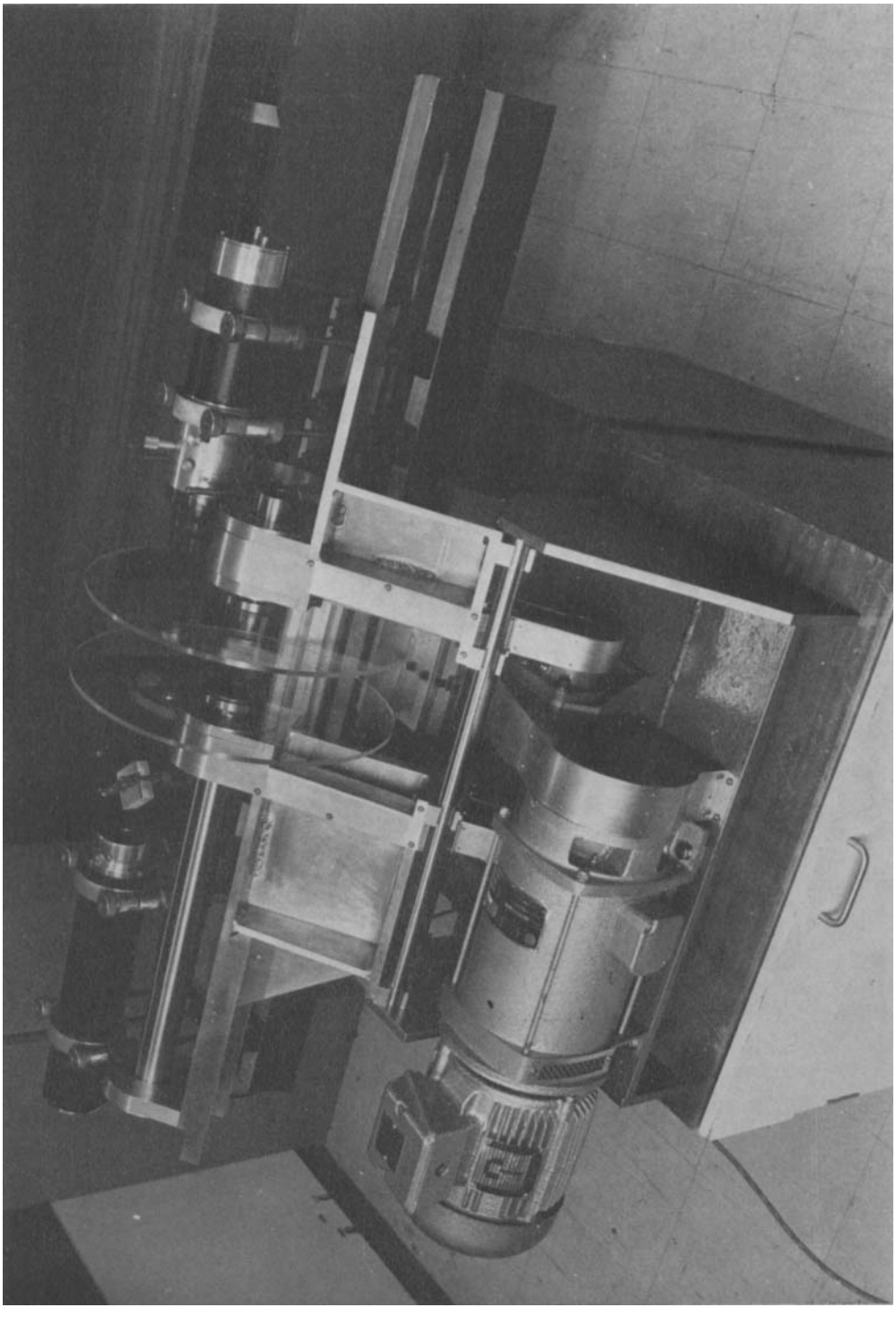

FIGURE 3. Laser-Doppler anemometer and rotating-disk assembly.